POLITECNICO DI TORINO
Repository ISTITUZIONALE

Multi-Layer Multi-User MIMO with Cylindrical Arrays under 3GPP 3D Channel Model for B5G/6G Networks

Original
Multi-Layer Multi-User MIMO with Cylindrical Arrays under 3GPP 3D Channel Model for B5G/6G Networks / Riviello, D.G., Tuninato, R., Garello, R.. - In: IEEE ACCESS. - ISSN 2169-3536. - ELETTRONICO. - 12:(2024), pp. 145753-145767. [10.1109/ACCESS.2024.3472489]

Availability:
This version is available at: 11583/2993550 since: 2024-10-21T20:18:35Z

Publisher:
IEEE

Published
DOI:10.1109/ACCESS.2024.3472489

Terms of use:

This article is made available under terms and conditions as specified in the corresponding bibliographic description in the repository

Publisher copyright

(Article begins on next page)

27 November 2026

IEEE Access
Multidisciplinary ⋮ Rapid Review ⋮ Open Access Journal

Received 10 September 2024, accepted 25 September 2024, date of publication 2 October 2024,
date of current version 15 October 2024.

Digital Object Identifier 10.1109/ACCESS.2024.3472489

RESEARCH ARTICLE

Multi-Layer Multi-User MIMO With Cylindrical Arrays Under 3GPP 3D Channel Model for B5G/6G Networks

DANIEL GAETANO RIVIELLO, (Member, IEEE), RICCARDO TUNINATO, (Graduate Student Member, IEEE), AND ROBERTO GARELLO, (Senior Member, IEEE)
Department of Electronics and Telecommunications, Politecnico di Torino, 10129 Turin, Italy
Corresponding author: Daniel Gaetano Riviello (daniel.riviello@polito.it)

ABSTRACT Massive MIMO technology has significantly enhanced the performance of 5G networks, and its potential is poised for further expansion in the upcoming 6G standard. Large antenna arrays at the transmitter, combined with multiple antennas at each user can enable multi-user multi-layer MIMO data transmission. In this paper, we study the potential benefits of a cylindrical array arrangement in a 3D scenario, compared to the conventional trisector planar array configuration. In fact, cylindrical arrays allow for more uniform coverage of the cell, don't suffer from beam broadening, and can mitigate the sector-edge problem. For this purpose, we assess the effectiveness of multi-user and multi-layer precoding and combining strategies using cylindrical arrays outfitted with both single and dual-polarized antenna elements, under the most recent 3GPP-compliant 3D channel model for 5G, and by taking into account impairments due to an imperfect channel estimation. Results and comparisons with planar arrays in terms of sum-rate, spectral efficiency and outage are provided for outdoor Line-of-Sight (LOS), outdoor Non-LOS, and indoor users. They highlight the benefits of using cylindrical arrays in realistic 3D scenarios, even when the planar arrays of the different sectors are coordinated to operate as a single array. This makes them an interesting solution for next-generation 6G networks.

INDEX TERMS Multi-user MIMO, cylindrical arrays, planar arrays, precoding, 5G, 6G.

I. INTRODUCTION

In the last ten years, there has been an exponential growth in the quantity of devices linked to the worldwide network, along with a surge in the number of services demanding higher data requirements. The current mobile network standard, 5G, has introduced innovative solutions that have been essential in meeting these emerging demands. 5G will evolve towards 6G through a series of technological innovations that will significantly enhance network capabilities. Key developments such as Reconfigurable Intelligent Surfaces (RIS) will enable dynamic control of the radio environment to improve signal strength and coverage [1], [2]. Non-Orthogonal Multiple Access (NOMA) will increase spectral efficiency by allowing multiple users to share the same frequency resources [3], [4], [5]. Green networks will focus on energy efficiency and sustainability, making networks more environmentally friendly [6], [7], [8]. Additionally, Non-Terrestrial Networks (NTN) will integrate satellite communication into the 6G architecture, providing global connectivity and coverage in remote areas [9], [10], [11], [12]. These advancements will lay the foundation for 6G, addressing the demands for higher data rates, low-latency applications, and more efficient use of spectrum and energy.

For Beyond 5G and 6G, the switch from Multiple Input Multiple Output (MIMO) systems to Massive MIMO systems, further enhanced through the utilization of new bands at higher frequencies, such as the millimeter wave (mmWave) spectrum, is one of the most promising solutions [13]. While the capabilities of MIMO systems are broadly recognized,

The associate editor coordinating the review of this manuscript and approving it for publication was Hassan Tariq Chattha.

© 2024 The Authors. This work is licensed under a Creative Commons Attribution 4.0 License.
For more information, see https://creativecommons.org/licenses/by/4.0/

thorough investigation is required to understand the particular conditions in which 5G and future systems will function.

In 5G systems, as opposed to LTE, relying on the assumption of 2D wave propagation is no longer sufficient, necessitating the implementation of suitable new 3D channel models. Thorough studies can be performed based on these channel models to examine the behaviour of novel methods and technologies. In our work, we focus on cylindrical and planar antenna arrays, which are essential for effectively utilizing the diversity of environments where cellular networks are placed. Given the significantly small size of each element, these antenna arrays in Massive MIMO systems can be formed by a high number of antennas. Through the implementation of Spatial Division Multiple Access (SDMA), antenna arrays can be exploited to offer distinct spatial channels to multiple users simultaneously using the same time and frequency resources, but inter-user interference must be handled.

Studying the comparison between the commonly utilized planar arrays and the cylindrical arrays on the transmitter side, i.e., the base station (BS), in a downlink (DL) Multi-User MIMO scenario, is the objective of this work. In the typical trisector cell, in which each of the 3 planar arrays covers one sector of 120°, beam broadening is particularly sensitive for those users lying at the edge of a sector. As opposed to planar arrays, cylindrical arrays are not affected by beam broadening and pattern deterioration when the beam is directed towards azimuth or elevation angles that are significantly away from broadside, thus they provide a more uniform coverage and they can eliminate the sector-edge problem.

A. PREVIOUS LITERATURE

Cylindrical Arrays: The theory of cylindrical antenna arrays is well established and can be found in several textbooks (see for example [14]). Arraycomm built and deployed such arrays 20 years ago, in Japan's 3G networks [15]. IEEE Spectrum presented massive MIMO with cylindrical arrays in 2017 [16]. More recently, the design and the architecture of cylindrical arrays have been widely studied [17], [18], [19], and possible applications to MIMO communication systems have been considered [19], [20], [21]. In [17], cylindrical antenna arrays are used for intelligent beam scanning, and in [18], the authors present an adaptive technique in which a subset of successive elements of a cylindrical array is activated each time. Choosing the subset relies on minimizing the angle between its broadside direction and the signal of interest's direction of arrival. In [19], the authors propose different architectures of cylindrical arrays for massive MIMO scenarios, namely, co-prime, nested, and sparse nested cylindrical arrays, and show that these sparse architectures could increase the channel capacity with fewer antenna elements. In [20] and [21], a hybrid uniform cylindrical array is designed for massive Internet of Things (IoT) networks the authors suggested a channel estimation method and a direction of arrival estimation algorithm specifically designed for the proposed hybrid array. An interesting application to High-altitude platform stations has been recently proposed in [22], [23]. We previously analyzed the behaviour of cylindrical arrays with an elementary directive channel model in [24], [25]. However, as far as the authors are aware, there have been no other investigations into the performance of such arrays in 5G Massive MIMO systems using a realistic 3D channel model, like the latest version of the 3GPP TR 38.901 spatial channel model [26], [27] and comparisons with planar arrays in this scenario. Table 1 presents a summary of the literature on cylindrical arrays.

TABLE 1. Some literature on cylindrical arrays.

Paper	Content
[14]	theory of cylindrical arrays
[15]	array deployment
[16]	massive MIMO
[17]	intelligent beam switching
[18]	adaptive activation
[19]	sparse architectures
[20]	hybrid arrays for massive IoT
[21]	channel estimation
[22], [23]	application to High-altitude platform stations
[24], [25]	beamforming
[28]	preliminary analysis on MU-MIMO
this paper	comprehensive study Multi-layer MU MIMO, 3D 3GPP models, comparison with planar arrays, LOS/NLOS, imperfect CSI, dual polarization

Precoding for Spatial Division Multiple Access: To achieve SDMA, it is necessary to implement appropriate precoding and combining schemes, where the main objective is to optimize the sum-rate of the users. An extensive analysis and comparison of different precoding techniques is provided in [29], where different classes of solutions are identified, as linear precoders, non-linear precoders, peak-to-average power ratio precoding algorithms and machine learning-based precoders. The optimal solution exists and can be found through non-linear Dirty Paper Coding [30], but its complexity is unbearable. Our interest is limited to linear precoders, due to their convenient trade-off between complexity and performance. Maximum-Ratio combining is a linear precoding technique which goal is to maximize the SNR to each user, while Zero-Forcing [31] tries to nullify the interference among them. The balance between these two solutions is the Minimum Mean Square Error (MMSE), analysed in [32]. In [33], a weighted MMSE (WMMSE) technique is designed for non-homogeneous SINR users, while in [34] an iterative WMMSE is derived to optimize a weighted sum-rate maximization problem. When users have multiple antennas at their disposal, a generalization of ZF, i.e., Block Diagonalization (BD) can be used [31]. BD is a sub-optimal low-complexity solution, and in [35] authors reduce its complexity even more with Jacket Matrix approximation. Nevertheless, there is a constraint on the MIMO system, since

the number of antennas at the transmitter must be greater than the number of the sum of the users' antennas. A very effective scheme that does not suffer from this limitation, namely Signal-to-Leakage plus Noise Ratio (SLNR) [36], [37], [38], is then chosen for our simulator. Differently from MMSE, the precoding vector must be computed for each user, but this process can be easily parallelized. In [39] the authors stated the equivalence between SLNR and MMSE, but this holds only for users with single antenna and homogeneous SNR, which is not our case. MMSE is instead implemented on the receiver side for the combiner [40], to make use of the antenna arrays of the User Terminals (UTs) and provide multi-layer capabilities (sometimes referred to multi-stream).

Array Architecture: In our implementation we are considering fully-digital precoding, i.e., an RF chain must be provided for each antenna element. However, costs, complexity and energy consumption are critical aspects of network design, and installing a large number of RF chains can become a problem, since an equivalent number of Digital-to-Analog converter (DAC) is required. This problem motivated many researchers to find alternative solutions. In order to reduce the number of RF chains, but to keep the advantages of many antenna elements, Hybrid Beamforming techniques have been explored, where both digital beamforming and analog beamforming are exploited [41]. Analog beamforming may reduce the degree of freedom on the beamforming capability, since usually only phase shifters may be tuned in the analog domain, which applies to the entire band. A comprehensive overview of hybrid beamforming techniques and architectures is presented in [42]. Heath et al. have followed a different track, by studying lower complexity DAC, as the 1-bit DAC [43], which permits the reduction of the complexity of MIMO systems, but they require longer training periods and may introduce some performance loss [44]. Since our interest is mainly on the system benchmark side, we are assuming no restrictions on the quantity of RF chains, keeping in mind that the actual system could require a hybrid beamformer, that can be still derived from a fully digital one [45], [46].

Channel State Information: Several beamforming techniques, as the ones adopted in our work, rely on the channel estimation, sometimes referred to as Channel State Information (CSI). Even if perfect channel knowledge is usually assumed for theoretical performance evaluation and software simulations, the impact of errors in the channel estimation process should be taken into consideration to better understand the system limitations. Thus, we perform our analysis also in the case of imperfect CSI, i.e., we consider the impact of channel coefficient estimation errors on the system performance, as in [47] and [48].

B. MOTIVATION AND METHODOLOGY

The motivation for this study stems from the critical need to optimize array configurations and transmission techniques as networks evolve towards Beyond 5G (B5G) and 6G. Cylindrical arrays, with their ability to provide full 360-degree coverage, offer significant potential for improving spectral efficiency and user experience in dense urban and indoor environments. Comparing these arrays with traditional planar arrays is essential to understanding their advantages and limitations. Furthermore, evaluating the impact of imperfect CSI, realistic antenna configurations, and different 3D propagation environments is crucial for designing robust systems. This research will provide valuable insights for advancing next-generation networks, contributing to more efficient solutions for beyond 5G and 6G networks.

As for the methodology, in this study, we employed the 3GPP 3D Channel Model to assess the performance of cylindrical arrays and compared it to planar arrays utilizing both sectorization and multi-sector joint transmission. We considered both single and dual-cross-polarized realistic antenna elements, examined the impact of imperfect CSI, and analyzed scenarios involving outdoor LOS/NLOS and indoor users. The results were evaluated in terms of sum-rate as a function of the number of users, spectral efficiency, per-user mean rate, and outage for different user types.

The analysis was conducted using a custom MATLAB simulator that includes all necessary elements, such as array configurations, precoding, and channel modeling. As an added value, we have made this simulator available as open-source software, enabling other researchers to replicate the results and further explore the analysis with additional findings.

C. CONTRIBUTION AND ORGANIZATION

In this work, we extend our preliminary study in [28], establishing a framework to evaluate a 5G New Radio system equipped with large antenna arrays that utilize SDMA techniques to significantly enhance wireless channel capacity. We thoroughly analyze the performance and conduct a comprehensive comparison between the commonly used trisector uniform planar arrays and the less explored cylindrical arrays under the latest 3GPP 3D channel model for 5G, across a wide range of conditions and scenarios. More in detail, this paper presents the following novelties w.r.t. [28]:

- We consider both single and dual-cross-polarized realistic antenna elements.
- We provide a detailed description of the 3GPP 3D channel model adopted for 5G.
- For the trisector planar array, we evaluate both sectorization with three independent planar arrays and sector cooperation, i.e., multi-sector joint transmission, where the three planar arrays coordinate to function as a single triangular prism array. Both configurations use full frequency reuse.
- We assess the impact of imperfect CSI on system performance to more accurately reflect real-world conditions, where channel estimation errors are common.
- We introduce a low-complexity, faster implementation of SLNR precoding.

- We account for both outdoor LOS/NLOS and indoor users.
- We present a comprehensive set of results, including system sum-rate as a function of the number of users to be served, spectral efficiency, per-user mean rate, and outage for outdoor LOS, indoor LOS, and non-LOS users.

The results show that cylindrical arrays exhibit excellent performance over realistic 3D scenarios. When compared to planar arrays, they offer more uniform cell coverage, do not experience beam broadening and effectively address the sector-edge problem. Consequently, they represent a compelling alternative for future advancements in beyond 5G and 6G networks.

Note: The complete Matlab code used to generate the paper's results is available at [49].

The structure of the paper is as follows. (Note: The mathematical models for planar and cylindrical arrays are well-documented in textbooks, such as [14], and clearly are not novel contributions of this paper. However, to enhance the accessibility of this open access paper and provide comprehensive notation, we have also included the relevant formulas in the Appendices.) The 3D scenario adopted in this paper is described in Sec. II, Array processing is established in Section III. The utilized 3GPP 3D channel model is outlined in Sec. IV. The considered Multi-User Multi-Layer MIMO strategy is introduced in Sec. V. An extensive set of numerical results are presented in Section VI, where planar and cylindrical solutions are compared in terms of sum-rate, spectral efficiency, user mean rate and outage. Finally, the conclusions are drawn in Section VII.

D. NOTATION

The symbol c^* represents the complex conjugate of the complex number c; lower-case boldface letters, such as $\mathbf{a}$, denote vectors; upper-case boldface letters $\mathbf{A}$ indicate matrices; $\mathbf{A}^\intercal$ and $\mathbf{A}^H$ represent the transpose and the Hermitian transpose of $\mathbf{A}$, respectively; $[\mathbf{A}]_{i,j}$ refers to the element located in the i-th row and j-th column of matrix $\mathbf{A}$; $\|\cdot\|_F^2$ is the Frobenius norm, and diag($\mathbf{A}$) is a vector composed of the diagonal elements of $\mathbf{A}$, whereas diag($[a_1, \ldots, a_L]$) is an $L \times L$ diagonal matrix containing the diagonal elements $[a_1, \ldots, a_L]$; vec($\cdot$) denotes the vectorization operation that combines the columns of an $N \times M$ matrix into a single $NM \times 1$ column vector; $\mathbf{1}_N$ signifies an $N \times 1$ column vector composed entirely of ones, while $\mathbf{0}_N$ denotes a $N \times 1$ all-zeros column vector.

II. 3D SCENARIO DESCRIPTION

Our analysis focuses on a cellular MIMO-OFDM network, where a BS uses a wideband mmWave channel containing Q subcarriers to communicate with multiple UTs. The analysis is conducted on a subband basis at the system level, with a carrier frequency f_c of 28 GHz. We consider a scenario where a single circular cell is positioned within an Urban Micro (UMi) street canyon environment [26]. The BS is situated at the cell's center, with a height $h_{BS} = 10$ m, and can use either Uniform Cylindrical Arrays (UCyA) or Uniform Planar Arrays (UPA). If UPA is used, the cell is divided into three sectors, each served by a different UPA, as shown in Fig. 1. In contrast, no sectorization is necessary when UCyA is used, as shown in Fig. 2.

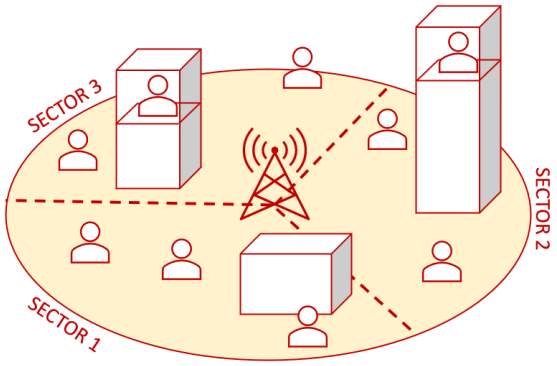

FIGURE 1. Circular cell site divided into three sectors for three uniform planar arrays.

We denote with $\mathcal{A} \subset \mathcal{R}^2$ the region where the circular cell is located, then the area of $\mathcal{A}$ is given by $|\mathcal{A}| = \pi R^2$, with R the radius (by default set to 100 m). To give more validation to our analysis, we exploit some results on the application of stochastic geometry to wireless networks [50], [51], [52], therefore, the UEs are placed randomly across the area $\mathcal{A}$ in accordance with a spatial homogeneous Poisson point process (PPP). The probability of having K users present in $\mathcal{A}$ is:

$$\Pr[M(\mathcal{A}) = K] = \frac{(\mu|\mathcal{A}|)^K}{K!} e^{-\mu|\mathcal{A}|} \tag{1}$$

where $M(\mathcal{A})$ is the random variable that denotes the count of users in a point process situated within the region $\mathcal{A}$ and μ (users/km^2) represents the average user density per unit area. Given that the process is homogeneous, μ remains constant and does not vary based on location. The K users derived from the Poisson process are conditionally independent and uniformly deployed within the circle, randomly positioned on circumferences at a specific distance ρ from BS given by $f_\rho(\rho) = 2\rho/R^2$, while the azimuth angle ϕ within the circle is generated through a uniform distribution ranging from 0 and 2π. In practical terms, for each Monte Carlo simulation we first generate a Poisson random variable K representing the number of users with mean parameter $\mu\mathcal{A}$, then given the K users, these are uniformly distributed in the circular area by definition of the spatial homogeneous PPP.

The position of the UTs also includes the z coordinate, namely the height h_{UT}, which is set at 1.5 m for outdoor users. The height of indoor users depends on the floor of the building where one UT is generated. The user's actual floor

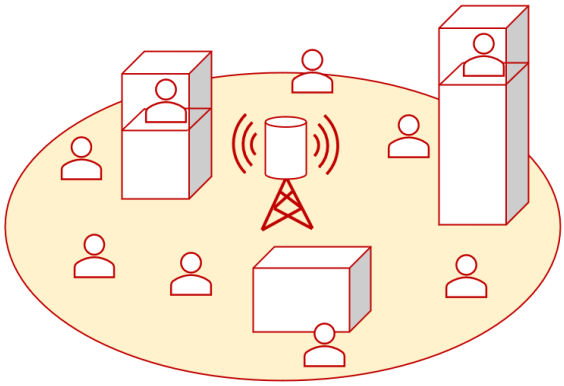

FIGURE 2. Circular cell site with a single cylindrical array.

$\mathrm{UT}_{\mathrm{floor}}$ is generated as $\mathrm{UT}_{\mathrm{floor}} \sim \mathcal{U}\,(1, \mathrm{floor}_{\max})$, where $\mathcal{U}(\cdot)$ is the discrete uniform distribution and $\mathrm{floor}_{\max} \sim \mathcal{U}\,(4, 8)$ is the number of floors of the building. The final height of the indoor user is then $h_{\mathrm{UT}} = 1.5 + 3\,\mathrm{UT}_{\mathrm{floor}}$.

III. ARRAY PROCESSING

This section presents the models for the antenna array and the pattern of the antenna element, applicable to both the BS and UT. We suppose that the BS can be outfitted with either a UCyA covering the entire azimuthal range or a trisector antenna type, which requires one UPA per sector. A uniform linear array (ULA), or a UPA, is installed in each of the two panels situated on the UT's opposite sides.

Appendix A contains a detailed description of the antenna arrays' system coordinates and orientation in space.

We denote with $F_\theta(\theta, \phi)$ and $F_\phi(\theta, \phi)$, the vertical and horizontal polarized field components of the antenna elements, respectively, where $\theta \in [0, 180°]$ is the zenith angle. They can be derived from the antenna 3D radiation power pattern of each antenna element as reported in Appendix B.

A. UNIFORM PLANAR ARRAY

Each sector of the cell is served by a different UPA of the BS with $N_t^{\mathrm{UPA}} = N_{ty} \times N_{tz}$ antenna elements equally polarized, where N_{ty} are the antennas along the y-axis and N_{tz} are the antennas along the z-axis. Each BS array is characterized by an index $s = (-1, 0, 1)$, associated with the particular sector the array is serving. The UPA with $s = 0$ is situated in the yz-plane (broadside to $\theta = 90°$, $\phi = 0°$), while the UPAs with $s = 1$ and $s = 2$ are broadside to $(\theta = 90°, \phi = 120°)$ and $(\theta = 90°, \phi = 240°)$, respectively. The UTs also adopt UPA, but with $N_r = N_{ry} \times N_{rz}$ antenna elements. A representation of a 4×2 UPA is provided in Fig. 3, where the antenna elements are cross-polarized. The antenna elements are uniformly spaced, with d_H and d_V the distances in horizontal and vertical direction, respectively [53]. Here we set these two distances equal to half the wavelength $d_H = d_V = \lambda/2$, where $\lambda = c/f_c$ representing the wavelength and c the light speed.

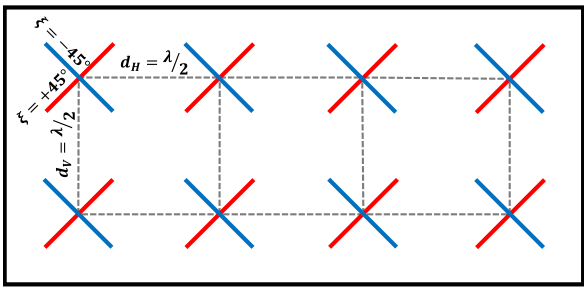

FIGURE 3. Uniform planar array consisting of antenna elements with cross-polarization. $N_{ty} = 4$, $N_{tz} = 2$.

For the antenna array factor $\mathbf{a}(\theta, \phi)$ of UPA, the individual element with index n_y along the y-axis and index n_z along the z-axis can be expressed as:

$$\exp\left(j\, 2\pi/\lambda \left[d_H n_y \sin\theta \sin\phi + d_V n_z \cos\theta\right]\right). \tag{2}$$

The derivation of this expression is reported in the Appendix C.

B. UNIFORM CYLINDRICAL ARRAY

The cylindrical array is composed by N_{tz} horizontal ring sub-arrays, each containing N_{tc} elements distributed uniformly around the circumference. On the circular arc a_c, the distance between elements is half the wavelength, obtained by setting a suitable ring radius:

$$R_c = \frac{\lambda N_{tc}}{4\pi}. \tag{3}$$

Along the vertical dimension, the spacing between successive rings is $d_V = \lambda/2$. Fig. 4 represents a cylindrical array with $N_{tz} = 4$ rings with $N_{tc} = 8$ cross-polarized antenna elements each.

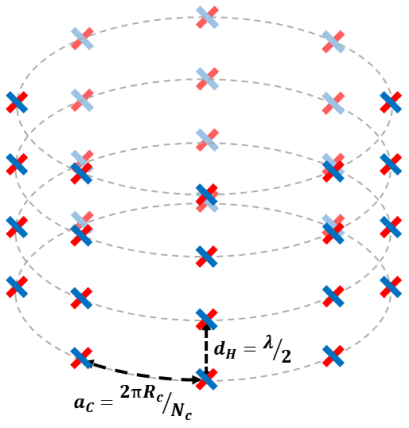

FIGURE 4. Uniform cylindrical array with cross-polarized antenna elements. $N_{tz} = 4$, $N_{tc} = 8$.

For the antenna array factor $\mathbf{a}(\theta, \phi)$ of UCyA, the specific element, indexed by n_c within a ring located in the $x-y$ plane,

TABLE 2. Comparison between planar and cylindrical transmitter antenna arrays.

Parameter	UPA	UCyA
Number of arrays per cell	3	1
Coverage per array [degrees]	120°	360°
Number of elements N_t per array	$N_{ty} \times N_{tz}$	$N_{tc} \times N_{tz}$ $N_{tc} = 3 \times N_{ty}$
Antenna spacing	$d_H = d_V = \lambda/2$	$a_c = d_V = \lambda/2$ $R_c = \frac{\lambda N_{tc}}{4\pi}$

and n_z indicating the ring's z-coordinate, can be expressed as follows:

$$\exp\left(j\, 2\pi/\lambda \left[R_c \sin\theta \cos\left(\phi - 2\pi n_c/N_{tc}\right) + d_V n_z \cos\theta\right]\right). \tag{4}$$

The derivation of this expression is reported in the Appendix D.

To ensure a fair comparison between the UCyA and UPA we take $N_t^{\text{UCyA}} = N_{tc} \times N_{tz} = 3N_{ty} \times N_{tz}$. Table 2 reports a summary of the main used parameters for UPA and UCyA antenna arrays, respectively.

IV. CHANNEL MODEL

In this section we outline the channel model adopted for the channel coefficient generation, which is based on the latest 3GPP 3D stochastic channel model described in TR 38.901 [26]. It is designed for the range of 0.5-100 GHz frequencies, and in particular for 5G mmWave massive MIMO communications, which require a 3-D channel model, since the wave propagation must be characterized both along the horizontal and vertical planes. In [27] we described this model in detail, whereas here we report a brief summary.

A. PROPAGATION CONDITIONS AND PATH LOSS CALCULATION

In case of an indoor user, the distance is the contribution of the outdoor 3D distance d_{3D-O}, the distance from the BS to the building, and the indoor 3D distance d_{3D-I}, the relative distance of the user k inside the building:

$$d_{3D} = d_{3D-O} + d_{3D-I}. \tag{5}$$

The propagation condition of each UT can be LOS or NLOS, and it is assigned based on a LOS probability P_{LOS}. [26, Tab. 7.4.2-1] in the 3GPP report provides all the detail to evaluate P_{LOS} for every distinct scenario under consideration. The proposed probability P_{LOS} is primarily influenced by the 2D distance between BS and UT, d_{2D} for O2O users and d_{2D-out} for O2I ones. In UMi and UMa environments the LOS probability is 1 for distances less than 18 meters, following which it diminishes with increasing distance.

The propagation condition affects the path loss (PL). [26, Tab. 7.4.1-1] of the 3GPP report illustrates the equations used to assess PL evaluation, for both UMi and UMa scenarios, encompassing both LOS and NLOS conditions. For UMi - Street canyon scenario, the PL of a LOS user is evaluated as

$$PL_{\text{LOS}} = \begin{cases} PL_1 & 10\,m \le d_{2D} \le d_{BP} \\ PL_2 & d_{BP} < d_{2D} \le 5\,km \end{cases} \tag{6}$$

with

$$PL_1 = 32.4 + 21\log_{10}(d_{3D}) + 20\log_{10}(f_c) \tag{7}$$

and

$$\begin{aligned} PL_2 = {} & 32.4 + 40\log_{10}(d_{3D}) + 20\log_{10}(f_c) \\ & + -9.5\log_{10}\left[(d_{BP})^2 + (h_{BS} - h_{UT})^2\right] \end{aligned} \tag{8}$$

where d_{BP} is the breakpoint distance ([26, Tab. 7.4.1-1] of the 3GPP report) and f_c is the carrier frequency in Hz.

For indoor users, the indoor path loss PL_{ind} is affected by additional losses due to the building walls and the obstacles inside the building:

$$PL_{ind} = PL_b + PL_{tw} + PL_{in} + \mathcal{N}(0, \sigma_P^2) \tag{9}$$

where PL_{tw} is the building penetration loss via the exterior wall and PL_b is the basic outside path loss. The inside loss, PL_{in}, is dependent on the depth within the building, and σ_P is the penetration loss's standard deviation. In order to calculate PL_{tw}, the 3GPP technical study recommends taking into account 70% concrete and 30% glass, whereas PL_{in} is determined by the 2D distance between the user and the interior wall of the building. The report includes a list of all the aforementioned metrics as well as the shadowing standard deviation σ_{SF} for each scenario.

For NLOS users, the σ_{SF} is larger, and PL_{NLOS} is selected as the maximum between PL_{LOS} and PL'_{NLOS}, the latter defined as:

$$\begin{aligned} PL'_{\text{NLOS}} = {} & 35.3\log_{10}(d_{3D}) + 22.4 \\ & + 21.3\log_{10}(f_c) - 0.3\log_{10}(h_{UT} - 1.5). \end{aligned} \tag{10}$$

B. LARGE SCALE PARAMETERS (LSP)

The LSPs characterize the user channel given the system geometry. In case of NLOS, six LSPs are generated: Delay Spread (DS), angular spreads of departure and arrival in both azimuth and zenith directions (ASA, ASD, ZSA, and ZSD) and shadow fading σ_{SF}. In case of LOS users, the Rician K-factor K_R is introduced, for a total of seven LSPs. All of these parameters are lognormal random variables, and [26, Tab. 7.5-6] of the report gives the means and variances of each parameter in a logarithmic scale. Certain correlations characterize the LSPs, which can be classified as:

- Intra-UT correlation: parameters correlation over the same link.
- Inter-UT correlation: parameters correlation over different links. It can be intra-cell and inter-cell.

The LSPs describe the main properties of the BS-UT link. Successively, the parameters that characterize each cluster and each ray contributing to the signal propagation are generated, namely the Small Scale Parameters (SSP).

C. SMALL SCALE PARAMETERS

This channel model is a Clustered Delay Line (CDL) Model, thus the received signal is the result of the contribution of N_{cl} clusters, each composed by M_{ray} rays. Each cluster and each ray has a certain direction in the 3D pace, represented as direction angle of departure in azimuth ϕ_{AoD} and zenith θ_{ZoD} from the UT, and direction angle of arrival in azimuth ϕ_{AoA} and zenith θ_{ZoA} toward the BS. Firstly, given a cluster n, its angular coordinates of arrival $\phi_{n,\text{AoA}}$ and $\theta_{n,\text{ZoA}}$ are generated as [26, eqs. 7.5-11 and 7.5-16] of the report. Then, the Azimuth of Arrival (AoA) and the Zenith of Arrival (ZoA) of the ray m composing the n cluster are derived as

$$\phi_{n,m,\text{AoA}} = \phi_{n,\text{AoA}} + C_{\text{ASA}}\alpha_m \tag{11}$$

and

$$\theta_{n,m,\text{ZoA}} = \theta_{n,\text{ZoA}} + C_{\text{ZSA}}\alpha_m \tag{12}$$

where C_{ASA} and C_{ZSA} are the cluster-wise RMS azimuth spread of arrival and the cluster-wise RMS zenith spread of arrival, respectively ([26, Tab. 7.5-6]); α_m is the per-ray offset ([26, Tab. 7.5-3]).

The computation of the angles corresponding to Azimuth and Zenith of Departure (AoD and ZoD, respectively) follows the same principle. In the case of LOS condition, the first cluster is the one representing the LOS link, and so its angular coordinates are computed according to the direction along which the UT points toward the BS. Finally, N_{cl} different cluster powers P_n and cluster delays τ_n are generated (7.5-6 and 7.5-2).

D. COEFFICIENT GENERATION

In the case of an OFDM subband, all cluster delays merge into a single tap. Then, the MIMO flat channel matrix element $[\mathbf{H}]_{u,v}^{\text{NLOS}}$ corresponding to the receiver's antenna element u and the transmitter's antenna element v can be calculated by using (17), as shown at the bottom of the next page, where $[\mathbf{a}_{n,m}^{rx}]_u$ is the index u of the array factor vector $\mathbf{a}(\theta_{n,m}^{\text{ZoA}}\phi_{n,m}^{\text{AoA}})$ for the receiver, while $[\mathbf{a}_{n,m}^{tx}]_v$ is the index v of the array factor vector $\mathbf{a}(\theta_{n,m}^{\text{ZoD}}, \phi_{n,m}^{\text{AoD}})$ for the transmitter. Moreover, $\{\Phi_{n,m}^{\theta\theta}\Phi_{n,m}^{\theta\phi}\Phi_{n,m}^{\phi\theta}\Phi_{n,m}^{\phi\phi}\}$ are the random initial phases for each ray m of each cluster n and for four different polarization combinations $(\theta\theta, \theta\phi, \phi\theta, \phi\phi)$, uniformly distributed between $-180°$ and $+180°$). Finally, $\kappa_{n,m}$ is the cross-polarization power ratio (XPR) for the m-th ray and the n-th cluster (7.5-21 in [26]).

If the user is in sight, the LOS path contribution is computed as in (18), as shown at the bottom of the next page.

The final matrix-valued channel impulse response, given by the sum of the NLOS and LOS contributions, is equal to:

$$\mathbf{H}^{\text{tot}} = \sqrt{\frac{1}{K_R+1}}\mathbf{H}^{\text{NLOS}} + \sqrt{\frac{K_R}{K_R+1}}\mathbf{H}^{\text{LOS}} \tag{13}$$

- In case of UPA, $\mathbf{H}^{\text{tot}}$ has size $N_r \times N_t^{\text{UPA}}$ for each BS sector and UT panel pair.
- In case of UCyA, $\mathbf{H}^{\text{tot}}$ has size $N_r \times N_t^{\text{UCyA}}$ for each UT panel.
- K_R is the Rician factor.
- Clearly, $\mathbf{H}^{\text{tot}} = \sqrt{1/(K_R+1)}\mathbf{H}^{\text{NLOS}}$ in case the user is not in sight.

E. IMPERFECT CHANNEL ESTIMATION

The application of beamforming techniques requires the knowledge of the wireless paths, i.e., the CSI, between the transmitter and the receiver. The acquisition of this knowledge is based on channel estimation, a crucial aspect in communication networks and even more in MIMO systems. In a time division duplex (TDD) scenario, channel reciprocity can be assumed. Therefore, in 5G NR, the channel estimation for beamforming can be performed either through Channel State Information Reference Signals (CSI-RS) or by using uplink sounding reference signals (SRS) transmitted for each user [54], [55]. Many studies on MIMO beamforming assume perfect channel estimation, but in actual scenarios the estimation is always affected by errors, as described in [56] and [57]. Thus, imperfect channel knowledge should be considered. The estimated channel for the generic k-th UT can be expressed as follows:

$$\widehat{\mathbf{H}}_k = \mathbf{H}_k + \mathbf{Z}_k \tag{14}$$

where $\mathbf{H}_k$ is the $N_r \times N_t$ true channel matrix for user k, as expressed in (13), while the entries of the $N_r \times N_t$ matrix $\mathbf{Z}_k$ are independently identically distributed (i.i.d) complex Gaussian random variables, i.e., $\text{vec}(\mathbf{Z}_k) \sim \mathcal{CN}\left(\mathbf{0}_{N_rN_t}, \zeta_k\mathbf{I}_{N_rN_t}\right)$, where $\mathbf{I}_{N_rN_t}$ is the $N_rN_t \times N_rN_t$ identity matrix, while ζ_k is a multiplicative factor resulting from the square root of the ratio between the mean power of the channel over the SNR of the SRS:

$$\zeta_k = \sqrt{\frac{\|\mathbf{H}_k\|_F^2}{N_t \cdot \text{SNR}_{\text{SRS}}}} \tag{15}$$

without loss of generality, we assume for each user k, $10\log_{10}\text{SNR}_{\text{SRS}} = 30$ dB. It is worth mentioning that we are not considering channel estimation improvements as time averaging (possible inside a time coherence block), neither we are exploiting the different time variability of large and small-scale fading factors, which could mitigate the effect of noise on the slow time-varying channel characteristic. Nevertheless, we still offer valuable insights on the harmful effect of errors on channel estimation, presenting results for both perfect and imperfect channel estimation.

V. MULTI-USER MULTI-LAYER MIMO SCHEME

In the proposed scenario, as described in Sec. II, the data transmission to each UT can carry L data layers, and comply with the condition $L \leq N_r$ and $LK \leq N_t$. The $L \times 1$ data symbol vector to be transmitted to the k-th user, here denoted by $\mathbf{s}_k$, has energy $\mathbb{E}[\mathbf{s}_k \mathbf{s}_k^H] = \frac{1}{L}\mathbf{I}_L$. Considering K users, the whole symbol vector to be transmitted is $\mathbf{s} = \left[\mathbf{s}_1^\intercal, \mathbf{s}_2^\intercal, \ldots, \mathbf{s}_K^\intercal\right]^\intercal$, composed by LK symbols. Thus, at the transmitter side a $N_t \times LK$ precoding matrix $\mathbf{W} = [\mathbf{W}_1, \mathbf{W}_2, \ldots, \mathbf{W}_K]$ is required, where $\mathbf{W}_k$ is the $N_t \times L$ precoder designed for user k. The precoder must comply with the power constraint $\|\mathbf{W}\|_F^2 \leq P_{\text{tot}}$, with P_{tot} the total transmitted power. The baseband representation of the received signal for the k-th user can be expressed in the following manner:

$$\mathbf{y}_k = \mathbf{H}_k \, \mathbf{x} = \mathbf{H}_k \sum_{i=1}^{K} \mathbf{W}_i \, \mathbf{s}_i + \mathbf{n}_k \tag{16}$$

where $\mathbf{n}_k \sim \mathcal{N}\left(0, \sigma_n^2 \mathbf{I}_{N_r}\right)$ is a $N_r \times 1$ noise vector with independent and identically distributed random variables, and σ_n^2 is the noise variance. Recalling from Sec. IV that each UT is equipped with two panels, $\mathbf{H}_k$ is selected among the two possible panel channel realizations over the highest energy metric. In the case of the trisectorized UPA scenario, the same selection criteria are extended for the 3 possible sectors (a total of 6 possible sector-panel pairs). In this work, no user scheduling or clustering is introduced, so the users are served over the same time-frequency resourced through spatial multiplexing, i.e. through SDMA beamforming techniques.

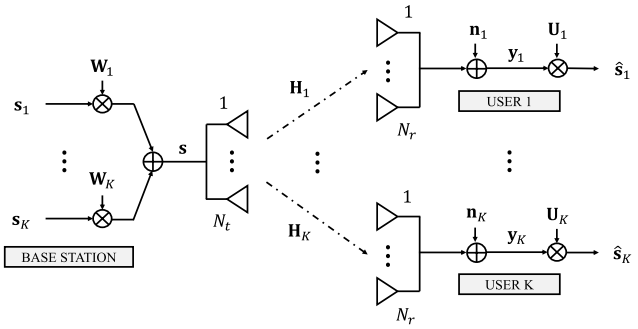

FIGURE 5. Multi-user multi-layer MIMO scheme.

A. LOW-COMPLEXITY SLNR PRECODING

At the transmitter side we rely on the well-known SLNR precoding scheme, which relies on the maximization of the signal-to-Leakage-plus-Noise ratio [36], where the leakage, defined as $\sum_{i=1,\, i\neq k}^{K} \|\mathbf{H}_i \mathbf{W}_k\|_F^2$, is the amount of interference that the k-th user introduces to all the others. The SLNR metric is therefore defined as:

$$\text{SLNR}_k = \frac{\|\mathbf{H}_k \mathbf{W}_k\|_F^2}{N_r \sigma_n^2 + \|\widetilde{\mathbf{H}}_k \mathbf{W}_k\|_F^2} \tag{19}$$

in which $\widetilde{\mathbf{H}}_k = [\mathbf{H}_1 \cdots \mathbf{H}_{k-1} \, \mathbf{H}_{k+1} \cdots \mathbf{H}_K]^\intercal$ is an extended $N_r\,(K-1) \times N_t$ channel matrix that only excludes user k. The optimal precoder for the SLNR metric is found in [37], [58], and [59], and it is derived from the solution of the generalized eigenvalue problem, i.e., the optimal $N_t \times L$ precoder designed for user k is made of L eigenvectors corresponding to the L largest eigenvalues of $\left(N_r \sigma_k^2 \mathbf{I}_{N_t} + \widetilde{\mathbf{H}}_k^H \widetilde{\mathbf{H}}_k\right)^{-1} \mathbf{H}_k^H \mathbf{H}_k$. Clearly, this approach is quite computationally expensive, since it requires K matrix inversions and K eigendecompositions. Therefore, we exploit the findings of [39] and we propose a low-complexity solution of SLNR precoding. In case of equal power allocation, we can implement multi-layer SLNR precoding in 3 steps:

1) We first apply the regularized zero-forcing technique to the global $KN_r \times N_t$ channel matrix $\mathbf{H} = [\mathbf{H}_1 \, \mathbf{H}_2 \cdots \mathbf{H}_K]^\intercal$ to generate the $N_t \times KN_r$ matrix $\widetilde{\mathbf{W}}$:

$$\widetilde{\mathbf{W}} = \mathbf{H}^H \left(\mathbf{H}\mathbf{H}^H + \frac{K\sigma_n^2}{P_{tot}} \mathbf{I}_{KN_r}\right)^{-1} \tag{20}$$

2) The second step is the normalization of the column of $\widetilde{\mathbf{W}}$:

$$\widehat{\mathbf{W}} = \widetilde{\mathbf{W}} \, \text{diag}\left(\frac{1}{\|\widetilde{\mathbf{w}}_1\|_2}, \frac{1}{\|\widetilde{\mathbf{w}}_2\|_2}, \ldots, \frac{1}{\|\widetilde{\mathbf{w}}_{KN_r}\|_2}\right) \tag{21}$$

3) Finally, $\widehat{\mathbf{W}} = \left[\widehat{\mathbf{W}}_1 \, \widehat{\mathbf{W}}_2 \cdots \widehat{\mathbf{W}}_K\right]$ can be partitioned into K matrices of size $N_t \times N_r$. Building on Eq. (16) of [39], which calculates the maximum SLNR for single-antenna receiving users, we can expand to encompass multiple-antenna receiving users with a vectorial notation. For each k-th user, the $N_t \times L$ precoding matrix $\mathbf{W}_k$ is built by selecting the L columns of $\widehat{\mathbf{W}}_k$ corresponding to the largest elements of the vector λ_k, computed as:

$$\lambda_k = \left(\mathbf{1}_{N_r} \oslash \left(\mathbf{1}_{N_r} - \text{diag}\left(\mathbf{H}_k \, \widehat{\mathbf{W}}_k\right)\right)\right) - \mathbf{1}_{N_r} \tag{22}$$

where $\oslash$ indicates the Hadamard elementwise division, and $\mathbf{1}_{N_r}$ is an $N_r \times 1$ column vector composed entirely of ones.

$$[\mathbf{H}]_{u,v}^{\text{NLOS}} = \sum_{n=1}^{N_{\text{cl}}} \sum_{m=1}^{M_{\text{ray}}} \sqrt{\frac{P_n}{M_{\text{ray}}}} \begin{bmatrix} F_{rx,u}^{\theta}(\theta_{n,m}^{\text{ZoA}}, \phi_{n,m}^{\text{AoA}}) \\ F_{rx,u}^{\phi}(\theta_{n,m}^{\text{ZoA}}, \phi_{n,m}^{\text{AoA}}) \end{bmatrix}^\intercal \begin{bmatrix} e^{(j\Phi_{n,m}^{\theta\theta})} & \sqrt{\kappa_{n,m}^{-1}} e^{(j\Phi_{n,m}^{\theta\phi})} \\ \sqrt{\kappa_{n,m}^{-1}} e^{(j\Phi_{n,m}^{\phi\theta})} & e^{(j\Phi_{n,m}^{\phi\phi})} \end{bmatrix} \begin{bmatrix} F_{tx,v}^{\theta}(\theta_{n,m}^{\text{ZoD}}, \phi_{n,m}^{\text{AoD}}) \\ F_{tx,v}^{\phi}(\theta_{n,m}^{\text{ZoD}}, \phi_{n,m}^{\text{AoD}}) \end{bmatrix} [\mathbf{a}_{n,m}^{rx}]_u [\mathbf{a}_{n,m}^{tx}]_v \tag{17}$$

$$[\mathbf{H}]_{u,v}^{\text{LOS}} = \exp\left(-j2\pi \frac{d_{3D}}{\lambda}\right) \begin{bmatrix} F_{rx,u}^{\theta}(\theta_{\text{LOS}}^{\text{ZoA}}, \phi_{\text{LOS}}^{\text{AoA}}) \\ F_{rx,u}^{\phi}(\theta_{\text{LOS}}^{\text{ZoA}}, \phi_{\text{LOS}}^{\text{AoA}}) \end{bmatrix}^\intercal \begin{bmatrix} 1 & 0 \\ 0 & -1 \end{bmatrix} \begin{bmatrix} F_{tx,v}^{\theta}(\theta_{\text{LOS}}^{\text{ZoD}}, \phi_{\text{LOS}}^{\text{AoD}}) \\ F_{tx,v}^{\phi}(\theta_{\text{LOS}}^{\text{ZoD}}, \phi_{\text{LOS}}^{\text{AoD}}) \end{bmatrix} [\mathbf{a}_{\text{LOS}}^{rx}]_u [\mathbf{a}_{\text{LOS}}^{tx}]_v. \tag{18}$$

B. MMSE COMBINING

At the UT side, when more antennas and more data layers are involved, a combiner scheme can be employed to mitigate the intra-user inter-layer interference [40]. Let us denote with $\mathbf{Z}_k = \mathbf{H}_k\,\mathbf{W}_k$ the equivalent channel matrix after precoding at the k-th user. A linear Minimum Mean Square Error (MMSE) combiner can be deployed to obtain a $L \times N_r$ combining matrix $\mathbf{U}_k$:

$$\mathbf{U}_k = \left(\mathbf{Z}_k^H\,\mathbf{Z}_k + \mathbf{G}_k\right)^{-1}\mathbf{Z}_k^H \tag{23}$$

with $\mathbf{G}_k$ the regularization matrix:

$$\mathbf{G}_k = \frac{\sigma^2}{P_{\text{tot}}}\mathbf{I}_L + \sum_{i=1,i\neq k}^{K}(\mathbf{H}_k\mathbf{W}_i)(\mathbf{H}_k\mathbf{W}_i)^H. \tag{24}$$

The signal vector estimation $\hat{\mathbf{s}}_k$ for user k following MMSE combining takes the following form:

$$\hat{\mathbf{s}}_k = \mathbf{U}_k\,\mathbf{H}_k\sum_{i=1}^{K}\mathbf{W}_i\,\mathbf{s}_i + \mathbf{U}_k\,\mathbf{n}_k. \tag{25}$$

The total power P_{tot} is equally divided among the total KL streams. Finally, the SINR of layer l for user k is:

$$\text{SINR}_{k,l} = \frac{\left|\mathbf{u}_{k,l}^{\intercal}\,\mathbf{H}_k\,\mathbf{w}_{k,l}\right|^2}{\left\|\mathbf{u}_{k,l}^{\intercal}\right\|^2\sigma_k^2 + \sum\limits_{\substack{d=1\\d\neq l}}^{L}\left|\mathbf{u}_{k,l}^{\intercal}\,\mathbf{H}_k\,\mathbf{w}_{k,d}\right|^2 + \sum\limits_{\substack{i=1\\i\neq k}}^{K}\sum_{d=1}^{L}\left|\mathbf{u}_{k,l}^{\intercal}\,\mathbf{H}_k\,\mathbf{w}_{i,d}\right|^2} \tag{26}$$

where $\mathbf{u}_{k,l}^{\intercal}$ refers to the l-th row of matrix $\mathbf{U}_k$ and $\left|\mathbf{u}_{k,l}^{\intercal}\,\mathbf{H}_k\,\mathbf{w}_{i,d}\right|^2$ quantifies the interference introduced by layer d of user i on layer l of user k. The spectral efficiency (SE) in bps/Hz for user k can be calculated as:

$$S_k = \sum_{l=1}^{L}\log_2(1+\text{SINR}_{k,l}). \tag{27}$$

In order to measure the performance of the system, serving multiple users in parallel, we finally define the sum-rate capacity as:

$$C_{\text{sum}} = B\sum_{k=1}^{K}S_k. \tag{28}$$

where B is the system frequency bandwidth.

Clearly, in case of imperfect channel estimation, both SLNR precoding and MMSE combining techniques are applied on the estimated channel matrices $\widehat{\mathbf{H}}_k$, $\forall k$, as defined in (14).

TABLE 3. Main scenario parameters.

Parameter	Value
Carrier frequency f_c	28 GHz
Bandwidth B	50 MHz
Number of OFDM subcarriers Q	792
Subband	60 kHz
Noise figure F	7 dB
Maximum TX power P_{tot}	50 dBm
Radius of the cell R	100 m
Network loading or user density μ	3500 users/km^2
Average number of UTs inside the cell	110 users
Polarization (pol)	single (dual)
Total antennas per BS UPA N_t^{UPA}	144 (288)
Total antennas per BS UCyA N_t^{UCyA}	432 (864)
Total antennas per UT N_r	2 (4)

VI. RESULTS AND COMPARISON BETWEEN CYLINDRICAL AND PLANAR ARRAYS

In this section we present an extensive set of numerical results obtained with different system configurations. We collect user statistics for both planar and cylindrical arrays, analyzing outdoor users in LOS, outdoor users in NLOS, and indoor users. The main system parameters, corresponding to a realistic 5G 3D scenario, are reported in Tab. 3. Notice that all radio frequency parameters are in accordance with 3GPP TS 38.101-2 [60].

A. SUM-RATE RESULTS

The first set of results we aim to analyze is the comparison of the sum-rate of the users, simultaneously served via SDMA, for different antenna arrays, number of polarizations and number of layers. Results for LOS, NLOS and indoor users are provided.

The curves in Fig. 6 are the sum-rates in Gbps as a function of increasing number of served users, for users in LOS conditions served by a 72 × 2 UPA (216 × 2 UCyA). There are three possible BS implementations:

- UPA with sectorization (UPA sect.) Each user is assigned to one sector only, and each UPA serves a different sector. The three UPAs transmit over the same frequency band (full frequency reuse), hence, inter-sector interference can affect the SINR. In each sector, one-third of the total number of users in the cell is served, on average.
- UPA with multi-sector joint transmission (UPA JT) This means that no sectorization is adopted, hence all users in the cell are jointly served by the three UPAs (sector cooperation).
- UCyA, which serves the whole cell (360° azimuthal coverage).

Analyzing the curves of Fig. 6 from the first approach, the behaviour of UCyA and UPA JT is similar, but UCyA can reach higher sum-rates as the number of users increases. For the second approach, UPA sect., performance starts to saturate much faster than the previous case, due to the inter-sector interference. Increasing the number of layers

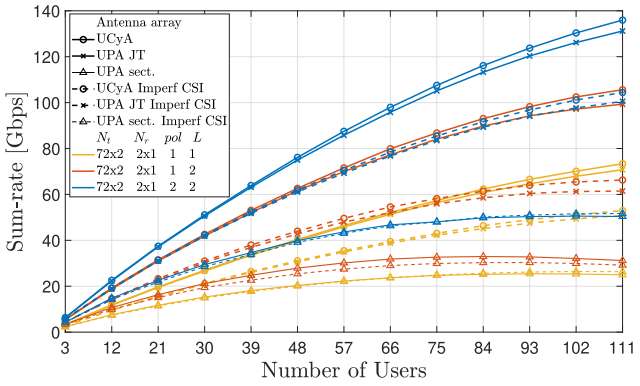

FIGURE 6. UCyA and UPA sum-rate for outdoor users in LOS condition. For UCyA, $N_t^{\text{UCyA}} = 3N_{ty} \times N_{tz}$.

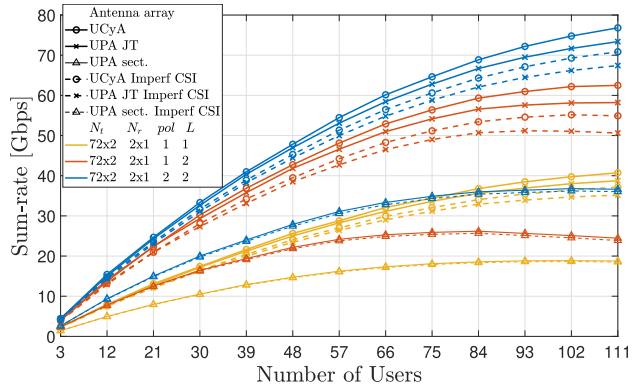

FIGURE 7. UCyA and UPA sum-rate for outdoor users in NLOS condition. For UCyA, $N_t^{\text{UCyA}} = 3N_{ty} \times N_{tz}$.

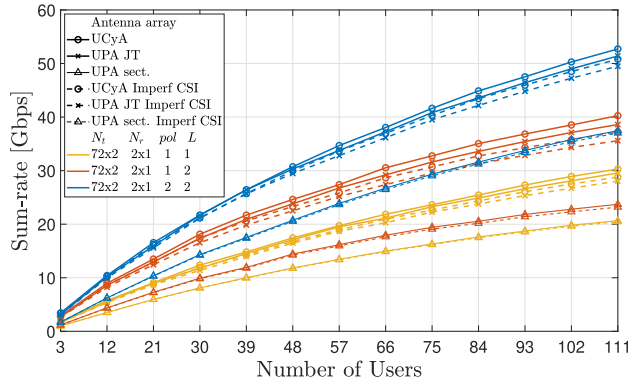

FIGURE 8. UCyA and UPA sum-rate for indoor users. For UCyA, $N_t^{\text{UCyA}} = 3N_{ty} \times N_{tz}$.

from 1 to 2 almost doubles the sum-rate, and higher gains can be achieved by having dual-polarized antenna elements, since the correlation experienced by the receiving antennas can be lower. In fact, when antennas are less correlated, it is easier to orthogonalize the data streams at the receiver side. The impact of imperfect CSI (dotted curves) is significant and it can reduce the maximum capacity of the system by a factor of about $25 - 45$ % depending on the configuration.

TABLE 4. Summary of sum-rate results from Figures 6, 7, and 8.

Condition	Antenna array	C_{sum} (perf. CSI) [Gbps]		C_{sum} (imperf. CSI) [Gbps]	
		$K = 50$	$K = 100$	$K = 50$	$K = 100$
LOS	UCyA A	41.7	69.3	32.1	50.6
	UCyA B	64.6	101.5	45.2	65.1
	UCyA C	78.6	128.9	63.8	100.1
	UPA JT A	41.2	67.2	31.6	48.9
	UPA JT B	63.5	96.5	43.9	61.1
	UPA JT C	77.4	124.9	62.9	96.9
	UPA sect. A	20.8	25.3	20.5	26.4
	UPA sect. B	28.4	32.2	25.9	30.0
	UPA sect. C	40.7	50.5	40	51.4
NLOS	UCyA A	26.3	39.5	24.7	36.2
	UCyA B	43.9	61.9	40.5	55.0
	UCyA C	49.3	74.2	46.6	68.8
	UPA JT A	25.7	37.8	24.1	34.5
	UPA JT B	42.9	58.0	39.4	51.1
	UPA JT C	48.3	71.2	45.6	65.8
	UPA sect. A	15.1	18.8	14.9	18.6
	UPA sect. B	22.6	25.	22.3	24.7
	UPA sect. C	28.6	36.7	28.1	36.1
Indoor	UCyA A	17.9	28.6	17.3	27.2
	UCyA B	25.2	38.1	23.9	35.4
	UCyA C	31.6	49.7	30.8	47.9
	UPA JT A	17.6	27.8	17.0	26.4
	UPA JT B	24.5	36.7	23.1	34.0
	UPA JT C	31.1	48.4	30.2	46.7
	UPA sect. A	12.2	19.6	12.1	19.4
	UPA sect. B	14.8	22.6	14.6	22.1
	UPA sect. C	21.4	35.3	21.2	34.9

A: pol = 1, L = 1 (yellow curves)
B: pol = 1, L = 2 (red curves)
C: pol = 2, L = 2 (blue curves)

For NLOS and indoor users, the results given the same array configurations are shown in Fig. 7 and Fig. 8, respectively. As might be expected, the sum-rate reduction is remarkable in both cases, compared to the previous LOS case. For the NLOS case, it is interesting to see how the gain given by the adoption of dual-polarized elements is still present but not as large as in the LOS case. The reason may lie in the fact that the NLOS case lacks the direct signal component, and thus the amount of correlation of the antenna elements is closer for the single and the dual polarizations options, with a lower impact on the performance. Table 4 reports a subset of the sum-rate results for 50 and 100 users, highlighting the impact of users' interference that limits the capacity growth, since it is not linear with the number of users.

B. SPECTRAL EFFICIENCY RESULTS

Given the same cylindrical/planar array configurations considered before, we want to investigate the results on the Cumulative Distribution Function (CDF) of the UT spectral efficiency when a very high number of users (about 110) are served. The curves of the CDF can be seen in Figs. 9, 10 and 11, for LOS, NLOS and indoor cases, respectively. The per-user SE behaviour is strictly related to the overall sum-rate. Here it can be appreciated how the users' SE are more spread away for the indoor case, and how the imperfect CSI is mostly limiting the users that would reach the highest capacities. Moreover, the UCyA benefits users at the lower

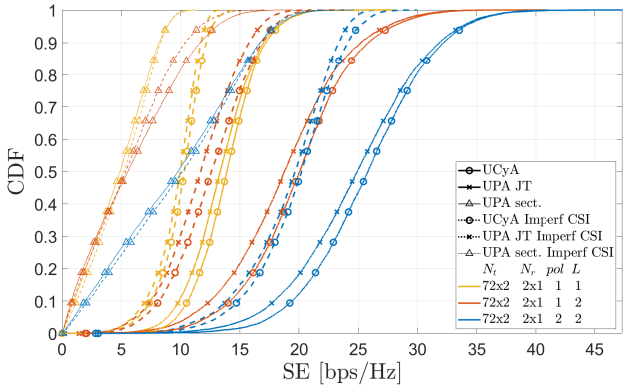

FIGURE 9. UCyA and UPA CDF curves of Spectral Efficiency for outdoor users in LOS condition. For UCyA, $N_t^{\text{UCyA}} = 3N_{ty} \times N_{tz}$.

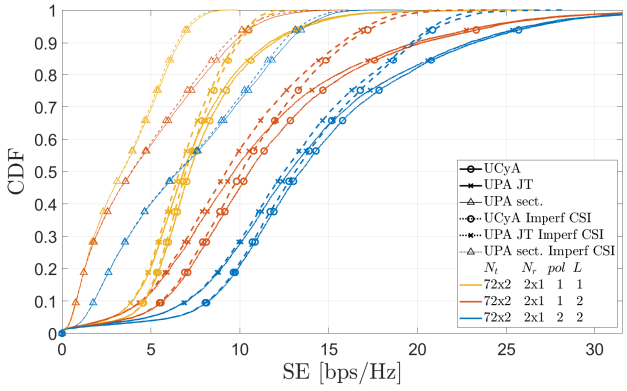

FIGURE 10. UCyA and UPA CDF curves of Spectral Efficiency for outdoor users in NLOS condition. For UCyA, $N_t^{\text{UCyA}} = 3N_{ty} \times N_{tz}$.

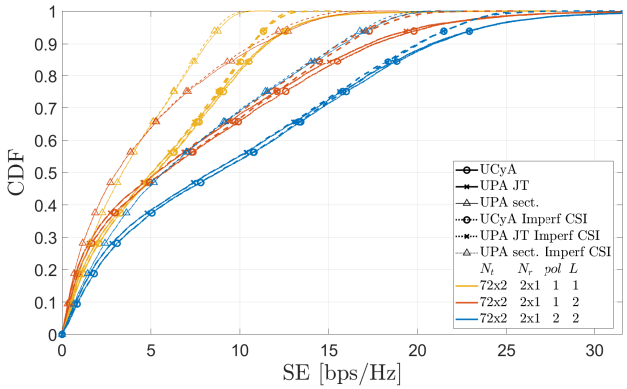

FIGURE 11. UCyA and UPA CDF curves of Spectral Efficiency for indoor users. For UCyA, $N_t^{\text{UCyA}} = 3N_{ty} \times N_{tz}$.

end of the SE levels, thereby enhancing system fairness. In line with the results of the sum-rate, also in this case the curves for the option with sectorization show substantially lower SE.

C. AVERAGE PER-USER RATE AND OUTAGE RESULTS

The last set of results is meant to evaluate the mean-rate of the UTs and their outage percentage, defined as the percentage of users experiencing an SINR lower than a

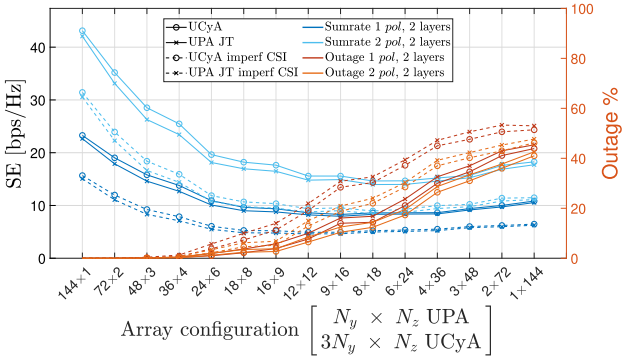

FIGURE 12. UCyA and UPA average per-user rate and outage vs. BS array configuration for outdoor users in LOS condition.

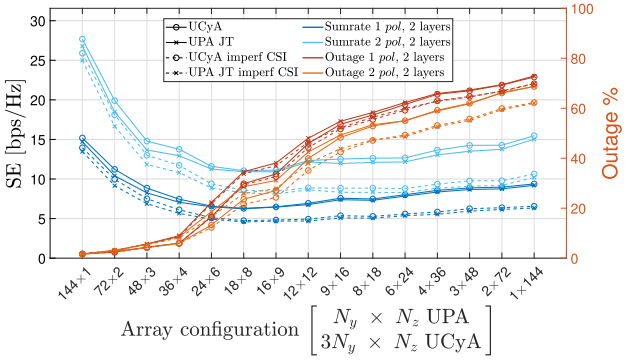

FIGURE 13. UCyA and UPA average per-user rate and outage vs. BS array configuration for outdoor users in NLOS condition.

certain threshold. This threshold is set in our simulations to 0 dB. The total number of antenna elements is fixed as $N_t^{\text{UPA}} = 144$ ($N_t^{\text{UCyA}} = 432$), but their arrangement is varied in several different configurations. In particular, we increase the number of elements along one of the two axes for the UPA with JT, vertical or horizontal, and correspondingly decrease the number of elements along the other. For the UCyA, the concept is the same but with the azimuth and zenith planes. The receiver array is configured as 2×1, and we take into account single and dual-polarized antenna elements with 2 and 4 layers, respectively. We omit to consider the sectorized case since it already proved to be much less effective than the solution based on sector cooperation. The results of these simulations for UTs in LOS condition can be seen in Fig. 12. The best mean-rates for the users can clearly be obtained when the antenna array is set with more elements along the the y-axis ($x - y$ plane). The reason behind these results is related to the spatial distribution of the users in the 3-D space, in which the users have the same height but different x and y coordinates. Thus, having more elements along the y-axis means having more spatial resolution along the $x - y$ plane than the z-plane, and so the users can be better spatially separated.

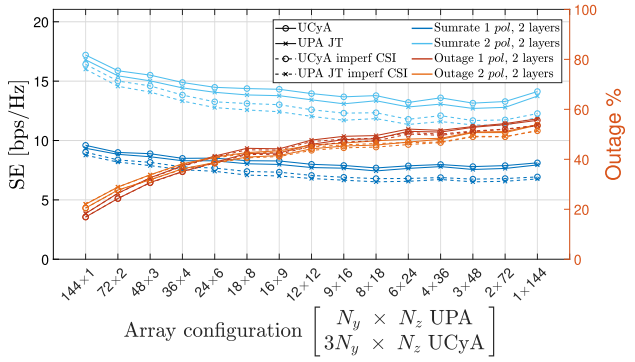

FIGURE 14. UCyA and UPA average per-user rate and outage vs. BS array configuration for indoor users.

In Fig. 13 the users are set in the NLOS case, and the behaviour of the curves is very similar, but the performance is worse than the LOS case, as we could have expected.

It is interesting to note that a quite different behaviour can be appreciated for indoor users in Fig. 14, where the difference in gains between arrays closer to a linear horizontal array is smaller, due to the fact that the users can be placed on different floors, and so the trade-off between spatial resolution along the $x-y$ plane and the z-plane is slightly more uniform.

In this case as well, the performance results from UCyA (circular marks) are superior to those from UPA Joint Transmission (squared marks). Results also show that the impact of imperfect CSI can be severe, limiting the maximum gains a Massive MIMO system could theoretically achieve. This underscores why channel estimation is a critical aspect in the application of SDMA precoding techniques to serve a large number of users.

VII. CONCLUSION

The scope of this paper was to consider a Multi-User Multi-Layer MIMO scheme based on SLNR precoding at the transmitter and MMSE combining at each User Terminal, and to present a thorough comparison between cylindrical and traditional planar arrays for a realistic 3GPP 3D scenario. In this analysis:

- We presented and discussed results in terms of sum-rate, spectral efficiency, per-user rate and outage.
- We provided results for LOS, NLOS and indoor users.
- We considered both single and dual-polarized antenna elements.
- For trisector planar arrays, we consider both sectorization with three independent planar arrays and sector cooperation.
- We analyzed the impact of imperfect CSI on the system performance.

All the results presented confirm that cylindrical arrays are very good for 3D scenarios, especially for users in less favorable conditions. They have excellent performance and, when compared with planar arrays, provide more uniform cell coverage, do not suffer from beam broadening, and effectively mitigate the sector-edge problem. Therefore, they represent a very interesting alternative for beyond 5G and 6G networks.

APPENDIX A
COORDINATES SYSTEMS AND ARRAY ORIENTATION

(Note: The mathematical models for planar and cylindrical arrays are well-documented in textbooks, such as [14]. However, to enhance the accessibility of this open access paper and provide comprehensive notation, we have also included the relevant formulas in this four appendices. The experienced reader can skip this part.)

In our work, the far-field patterns and polarization of the antenna are specified in the Local Coordinate System (LCS). However, the positions of the BS and the UTs, as well as the orientation of their arrays, are defined in the Global Coordinate System (GCS).

Let us consider a point (x, y, z) in the unit sphere, characterized in Cartesian coordinates by the position vector $\mathbf{r}(\theta, \phi) = [\sin\theta\cos\phi,\ \sin\theta\sin\phi,\ \cos\theta]^{\mathsf{T}}$. This GCS representation is a function of θ and ϕ, and the corresponding LCS representation is obtained as $\mathbf{R}^{-1}\mathbf{r}$, where $\mathbf{R}$ is the rotation matrix defined as

$$\begin{aligned}\mathbf{R} &= \mathbf{R}_z(\alpha)\mathbf{R}_y(\beta)\mathbf{R}_x(\gamma)\\ &== \begin{bmatrix}\cos\alpha & -\sin\alpha & 0\\ \sin\alpha & \cos\alpha & 0\\ 0 & 0 & 1\end{bmatrix}\begin{bmatrix}\cos\beta & 0 & \sin\beta\\ 0 & 1 & 0\\ -\sin\beta & 0 & \cos\beta\end{bmatrix}\\ &\quad\times\begin{bmatrix}1 & 0 & 0\\ 0 & \cos\gamma & -\sin\gamma\\ 0 & \sin\gamma & \cos\gamma\end{bmatrix}\end{aligned} \tag{29}$$

After this transformation, the azimuth angle ϕ' and zenith angle θ' in LCS can be obtained as follows

$$\theta'(\alpha,\beta,\gamma;\theta,\phi) = \arccos\left([0,\ 0,\ 1]\,\mathbf{R}^{-1}\mathbf{r}\right) \tag{30}$$

$$\phi'(\alpha,\beta,\gamma;\theta',\phi') = \arg\left([1,\ j,\ 0]\,\mathbf{R}^{-1}\mathbf{r}\right). \tag{31}$$

Regarding the orientation of an antenna array in space, it is described by three parameters: the bearing angle α, the down tilt angle β and the slant angle γ, all calculated from the GCS. For the BS arrays, both β and γ are set to 0, and α depends on the type of array. In case of UCyA α is set to 0, while for UPA there can be 3 different orientations, depending on the sector, so $\alpha = s120°$ where $s = -1, 0, 1$. For the UT, the orientation of the first panel with respect to the GCS is determined by:

$$\begin{aligned}\alpha_{\mathrm{UT}}^{(1)} &\sim \mathcal{U}(-180°, +180°)\\ \beta_{\mathrm{UT}} &\sim \mathcal{N}(\mu_\beta, \sigma_\beta^2)\\ \gamma_{\mathrm{UT}} &\sim \mathcal{N}(\mu_\gamma, \sigma_\gamma^2)\end{aligned} \tag{32}$$

where $\mathcal{N}(\cdot)$ denotes the continuous normal distribution, $\mu_\beta = \mu_\gamma = 0°$ and $\sigma_\beta^2 = \sigma_\gamma^2 = 36°$. The second panel has the same β_{UT} and γ_{UT}, while $\alpha_{\mathrm{UT}}^{(2)} = 180° + \alpha_{\mathrm{UT}}^{(1)}$.

APPENDIX B
ANTENNA RADIATION PATTERN AND POLARIZATION

In [26, Tab. 7.3-1] the expressions of the 3D radiation power pattern of each BS antenna element $A(\theta', \phi')$ are detailed in LCS. In a more compact form, they can be rewritten as

$$A_{\text{dB}}(\theta', \phi') = \begin{cases} -A_{\max} & \text{if } (\phi'/\phi_{3\text{dB}})^2 + (\widetilde{\theta}'/\theta_{3\text{dB}})^2 > \dfrac{A_{\max}}{12} \\ -12\left[(\phi'/\phi_{3\text{dB}})^2 + (\widetilde{\theta}'/\theta_{3\text{dB}})^2\right] & \text{otherwise} \end{cases} \tag{33}$$

where $\widetilde{\theta}' = \theta' - 90°$, $\theta' \in [0°, 180°]$ and $\phi' \in [-180°, 180°]$. $A_{\max} = 30$ dB is the maximum loss and $\theta_{3\text{dB}} = \phi_{3\text{dB}} = 65°$ are the angles corresponding to the half-power beamwidth. Finally, the highest directional gain of an antenna element, denoted as $G_{\text{E,max}}$, is equal to 8 dBi.

The 3D radiation pattern for the antenna array element of the UT is the same of (33), but with different parameters: $A_{\max} = 25$ dB, $G_{\text{E,max}} = 5$ dBi and $\theta_{3\text{dB}} = \phi_{3dB} = 90°$ [61].

The connection between the power pattern and the vertical and horizontal polarized field components in LCS, $F'_{\theta'}$ and $F'_{\phi'}$ respectively, is:

$$A'(\theta', \phi') = |F'_{\theta'}(\theta', \phi')|^2 + |F'_{\phi'}(\theta', \phi')|^2. \tag{34}$$

The polarization of the antenna elements determines how the two polarized field components are defined. For single polarized antenna elements only the vertical polarized field component is active, so $F'_{\phi'} = 0$ and $F'_{\theta'} = \sqrt{A'(\theta', \phi')}$. In case of dual-polarized antenna elements they can be expressed as:

$$F'_{\phi'} = \sqrt{A'(\theta', \phi')}\cos(\xi) \quad F'_{\phi'} = \sqrt{A'(\theta', \phi')}\sin(\xi) \tag{35}$$

where ξ is the polarization slant angle and $\xi = \pm 45°$ corresponds to a pair of cross polarized antenna elements. The transformation of the polarized field components from LCS to GCS is:

$$\begin{bmatrix} F_\theta(\theta, \phi) \\ F_\phi(\theta, \phi) \end{bmatrix} = \begin{bmatrix} +\cos\psi & -\sin\psi \\ +\sin\psi & +\cos\psi \end{bmatrix} \begin{bmatrix} F'_{\theta'}(\theta', \phi') \\ F'_{\phi'}(\theta', \phi') \end{bmatrix} \tag{36}$$

where the angle ψ can be computed as:

$$\psi = \arg\left(\begin{matrix} (\sin\gamma\cos\theta\sin(\phi - \alpha) + \\ +\cos\gamma(\cos\beta\sin\theta - \sin\beta\cos\theta\cos(\phi - \alpha))) + \\ +j(\sin\gamma\cos(\phi - \alpha) + \sin\beta\cos\gamma\sin(\phi - \alpha)) \end{matrix} \right). \tag{37}$$

APPENDIX C
UNIFORM PLANAR ARRAY FACTOR

The UPA array factor can be determined by taking the scalar product of the location matrix of the antenna elements $\mathbf{P}_{\text{UPA}}$ and the spherical unit vector $\mathbf{r}$, which corresponds to the azimuth angle ϕ and zenith angle θ in GCS defined by the UT position:

$$\mathbf{a}(\theta, \phi) = \exp\left(\frac{j2\pi(\mathbf{P}_{\text{UPA}} \cdot \mathbf{r})}{\lambda}\right) \tag{38}$$

$\mathbf{P}_{\text{UPA}}$ is a matrix with dimensions of $3 \times N_t^{\text{UPA}}$, where each row represents the position of the antenna elements along one of the three coordinates (x, y, z), rotated w.r.t. the three rotation angles (α, β, γ), through the product with the rotation matrix $\mathbf{R}$:

$$\mathbf{P}_{\text{UPA}} = \mathbf{R}\begin{bmatrix} \mathbf{0}_N^\intercal \\ \text{vec}\left(\mathbf{d}_y \cdot \mathbf{1}_{N_{tz}}^\intercal\right)^\intercal \\ \text{vec}\left(\mathbf{1}_{N_{ty}} \cdot \mathbf{d}_z^\intercal\right)^\intercal \end{bmatrix} \tag{39}$$

where the position vectors $\mathbf{d}_y$ and $\mathbf{d}_z$ are determined by the relative positions of each antenna element along the y-axis and z-axis respectively:

$$\mathbf{d}_y = d_H\left[-N_y/2, \ \ldots, \ +N_y/2\right]^\intercal \tag{40}$$

$$\mathbf{d}_z = d_V\left[-N_z/2, \ \ldots, \ +N_z/2\right]^\intercal \tag{41}$$

The spherical unit vector $\mathbf{r}$ is calculated based on the Zenith of Departure θ_{ZoD} and Azimuth of Departure ϕ_{AoD} for the transmitter, as well as the Zenith of Arrival θ_{ZoA} and Azimuth of Arrival ϕ_{AoA} for the receiver. The vector $\mathbf{r}$ is then $\mathbf{r}_{tx} = \mathbf{r}(\theta_{\text{ZoD}}, \phi_{\text{AoD}})$ and $\mathbf{r}_{rx} = \mathbf{r}(\theta_{\text{ZoA}}, \phi_{\text{AoA}})$, respectively.

APPENDIX D
UNIFORM CYLINDRICAL ARRAY FACTOR

As for the array factor of the planar array, it is defined as shown in (38). However, for the UCyA the location matrix of the antenna array elements must consider the distinct shape, and thus it is defined as:

$$\mathbf{P}_{\text{UCyA}} = \mathbf{R}\begin{bmatrix} \text{vec}\left(\mathbf{d}_{c_x} \cdot \mathbf{1}_{N_z}^\intercal\right)^\intercal \\ \text{vec}\left(\mathbf{d}_{c_y} \cdot \mathbf{1}_{N_z}^\intercal\right)^\intercal \\ \text{vec}\left(\mathbf{1}_{N_c} \cdot \mathbf{d}_z^\intercal\right)^\intercal \end{bmatrix} \tag{42}$$

The coordinate vector along the z-axis, denoted as $\mathbf{d}_z$ remains identical to the one defined in the UPA, as shown in (41), whereas the vectors $\mathbf{d}_{c_x}$ and $\mathbf{d}_{c_y}$ represent the x and y coordinates respectively for each antenna element situated in a circle with radius equal to R_c, as defined by:

$$\mathbf{d}_{c_x} = R_c\cos\left(2\pi/\lambda\left[0, \ \ldots, \ N_{tc} - 1\right]\right) \tag{43}$$

$$\mathbf{d}_{c_y} = R_c\sin\left(2\pi/\lambda\left[0, \ \ldots, \ N_{tc} - 1\right]\right). \tag{44}$$

ACKNOWLEDGMENT

An earlier version of this paper was presented in part at the IEEE 20th Consumer Communications and Networking Conference (IEEE CCNC 2023) [10.1109/CCNC51644.2023.10060861].

REFERENCES

[1] S. Basharat, S. A. Hassan, H. Pervaiz, A. Mahmood, Z. Ding, and M. Gidlund, "Reconfigurable intelligent surfaces: Potentials, applications, and challenges for 6G wireless networks," *IEEE Wireless Commun.*, vol. 28, no. 6, pp. 184–191, Dec. 2021.

[2] E. Shi, J. Zhang, H. Du, B. Ai, C. Yuen, D. Niyato, K. B. Letaief, and X. Shen, "RIS-aided cell-free massive MIMO systems for 6G: Fundamentals, system design, and applications," *Proc. IEEE*, vol. 112, no. 4, pp. 331–364, Apr. 2024.

[3] Y. Liu, S. Zhang, X. Mu, Z. Ding, R. Schober, N. Al-Dhahir, E. Hossain, and X. Shen, "Evolution of NOMA toward next generation multiple access (NGMA) for 6G," *IEEE J. Sel. Areas Commun.*, vol. 40, no. 4, pp. 1037–1071, Apr. 2022.
[4] X. Mu, Z. Wang, and Y. Liu, "NOMA for integrating sensing and communications towards 6G: A multiple access perspective," *IEEE Wireless Commun.*, vol. 31, no. 3, pp. 1–8, Jan. 2023, doi: 10.1109/MWC.015.2200559.
[5] A. Andrawes, R. Nordin, and N. F. Abdullah, "Energy-efficient downlink for non-orthogonal multiple access with SWIPT under constrained throughput," *Energies*, vol. 13, no. 1, p. 107, Dec. 2019.
[6] T. Huang, W. Yang, J. Wu, J. Ma, X. Zhang, and D. Zhang, "A survey on green 6G network: Architecture and technologies," *IEEE Access*, vol. 7, pp. 175758–175768, 2019.
[7] R. Salama, F. Al-Turjman, D. Bordoloi, and S. P. Yadav, "Wireless sensor networks and green networking for 6G communication—An overview," in *Proc. Int. Conf. Comput. Intell., Commun. Technol. Netw. (CICTN)*, Apr. 2023, pp. 830–834.
[8] Z. Albataineh, A. Andrawes, N. Abdullah, and R. Nordin, "Energy-efficient beyond 5G multiple access technique with simultaneous wireless information and power transfer for the factory of the future," *Energies*, vol. 15, no. 16, p. 6059, Aug. 2022.
[9] M. Giordani and M. Zorzi, "Non-terrestrial networks in the 6G era: Challenges and opportunities," *IEEE Netw.*, vol. 35, no. 2, pp. 244–251, Mar. 2021.
[10] G. Araniti, A. Iera, S. Pizzi, and F. Rinaldi, "Toward 6G non-terrestrial networks," *IEEE Netw.*, vol. 36, no. 1, pp. 113–120, Jan. 2022.
[11] G. M. Capez, M. A. Cáceres, R. Armellin, C. P. Bridges, J. A. Fraire, S. Frey, and R. Garello, "On the use of mega constellation services in space: Integrating LEO platforms into 6G non-terrestrial networks," *IEEE J. Sel. Areas Commun.*, early access, Sep. 12, 2024, doi: 10.1109/JSAC.2024.3459078.
[12] M. R. Dakkak, D. G. Riviello, A. Guidotti, and A. Vanelli-Coralli, "Evaluation of multi-user multiple-input multiple-output digital beamforming algorithms in B5G/6G low Earth orbit satellite systems," *Int. J. Satell. Commun. Netw.*, pp. 1–17, Aug. 2023.
[13] W. Roh, J.-Y. Seol, J. Park, B. Lee, J. Lee, Y. Kim, J. Cho, K. Cheun, and F. Aryanfar, "Millimeter-wave beamforming as an enabling technology for 5G cellular communications: Theoretical feasibility and prototype results," *IEEE Commun. Mag.*, vol. 52, no. 2, pp. 106–113, Feb. 2014.
[14] E. Björnson, J. Hoydis, and L. Sanguinetti, *Massive MIMO Networks: Spectral, Energy, and Hardware Efficiency* (Foundations and Trends in Signal Processing). Norwell, MA, USA: Now Publishers, 2017.
[15] EE. Björnson. (2017). *Cellular Multi-User MIMO: A Technology Whose Time Has Come*. Wireless Future. [Online]. Available: https://ma-mimo.ellintech.se/2016/11/11/cellular-multi-user-mimo-a-technology-whose-time-has-come/
[16] A. Nordrum and C. Kaisten, "5G bytes: Massive MIMO explained," IEEE Spectrum, Jun. 2017. Accessed: Oct. 3, 2024. [Online]. Available: https://spectrum.ieee.org/5g-bytes-massive-mimoexplained
[17] V. C. Misra, L. N. Merugu, R. V. H. Prasad, T. G. K. Murty, and O. K. Singh, "Beam switching cylindrical array antenna system for communication," *Defence Sci. J.*, vol. 48, no. 4, pp. 403–412, Jan. 1998.
[18] T. N. Kaifas and J. N. Sahalos, "Design and performance aspects of an adaptive cylindrical beamforming array," *IEEE Antennas Propag. Mag.*, vol. 54, no. 1, pp. 51–65, Feb. 2012.
[19] N. Wu, F. Zhu, and Q. Liang, "Evaluating spatial resolution and channel capacity of sparse cylindrical arrays for massive MIMO," *IEEE Access*, vol. 5, pp. 23994–24003, 2017.
[20] Z. Lin, T. Lv, W. Ni, J. A. Zhang, and R. P. Liu, "Nested hybrid cylindrical array design and DoA estimation for massive IoT networks," *IEEE J. Sel. Areas Commun.*, vol. 39, no. 4, pp. 919–933, Apr. 2021.
[21] Z. Lin, T. Lv, W. Ni, J. A. Zhang, and R. P. Liu, "Tensor-based multi-dimensional wideband channel estimation for mmWave hybrid cylindrical arrays," *IEEE Trans. Commun.*, vol. 68, no. 12, pp. 7608–7622, Dec. 2020.
[22] K. Tashiro, K. Hoshino, and A. Nagate, "Cylindrical massive MIMO system for HAPS: Capacity enhancement and coverage extension," in *Proc. IEEE 93rd Veh. Technol. Conf. (VTC-Spring)*, Apr. 2021, pp. 1–6.
[23] R. Shafie, M. J. Omidi, O. Abbasi, and H. Yanikomeroglu, "MIMO-NOMA enabled sectorized cylindrical massive antenna array for HAPS with spatially correlated channels," *IEEE Trans. Wireless Commun.*, early access, Jul. 23, 2024, doi: 10.1109/TWC.2024.3426521.
[24] D. G. Riviello and R. Garello, "Implementation of 5G beamforming techniques on cylindrical arrays," in *Proc. IEEE-APS Topical Conf. Antennas Propag. Wireless Commun. (APWC)*, Sep. 2019, pp. 413–418.
[25] D. G. Riviello and F. D. Stasio, "5G beamforming implementation and trade-off investigation of cylindrical array arrangements," in *Proc. 22nd Int. Symp. Wireless Pers. Multimedia Commun. (WPMC)*, Nov. 2019, pp. 1–6.
[26] *Study on Channel Model for Frequencies From 0.5 to 100 GHz (Release 16) V16.1.0*, Standard TR 38.901, 3GPP, Sophia Antipolis, France, 2020.
[27] D. G. Riviello, F. Di Stasio, and R. Tuninato, "Performance analysis of multi-user MIMO schemes under realistic 3GPP 3-D channel model for 5G mmWave cellular networks," *Electronics*, vol. 11, no. 3, p. 330, Jan. 2022.
[28] D. G. Riviello, R. Tuninato, and R. Garello, "Assessment of MU-MIMO schemes with cylindrical arrays under 3GPP 3D channel model for B5G networks," in *Proc. IEEE 20th Consum. Commun. Netw. Conf. (CCNC)*, Jan. 2023, pp. 769–774.
[29] M. A. Albreem, A. H. A. Habbash, A. M. Abu-Hudrouss, and S. S. Ikki, "Overview of precoding techniques for massive MIMO," *IEEE Access*, vol. 9, pp. 60764–60801, 2021.
[30] M. H. M. Costa, "Writing on dirty paper," *IEEE Trans. Inf. Theory*, vol. IT-29, no. 3, pp. 439–441, May 1983.
[31] Q. H. Spencer, A. L. Swindlehurst, and M. Haardt, "Zero-forcing methods for downlink spatial multiplexing in multiuser MIMO channels," *IEEE Trans. Signal Process.*, vol. 52, no. 2, pp. 461–471, Feb. 2004.
[32] C. B. Peel, B. M. Hochwald, and A. L. Swindlehurst, "A vector-perturbation technique for near-capacity multiantenna multiuser communication—Part I: Channel inversion and regularization," *IEEE Trans. Commun.*, vol. 53, no. 1, pp. 195–202, Jan. 2005.
[33] D. H. Nguyen and T. Le-Ngoc, "MMSE precoding for multiuser MISO downlink transmission with non-homogeneous user SNR conditions," *EURASIP J. Adv. Signal Process.*, vol. 2014, no. 1, pp. 1–12, Dec. 2014, Art. no. 85.
[34] S. S. Christensen, R. Agarwal, E. De Carvalho, and J. M. Cioffi, "Weighted sum-rate maximization using weighted MMSE for MIMO-BC beamforming design," *IEEE Trans. Wireless Commun.*, vol. 7, no. 12, pp. 4792–4799, Dec. 2008.
[35] M. H. A. Khan, K. M. Cho, M. H. Lee, and J.-G. Chung, "A simple block diagonal precoding for multi-user MIMO broadcast channels," *EURASIP J. Wireless Commun. Netw.*, vol. 2014, no. 1, pp. 1–8, Dec. 2014, Art. no. 95.
[36] A. Tarighat, M. Sadek, and A. H. Sayed, "A multi user beamforming scheme for downlink MIMO channels based on maximizing signal-to-leakage ratios," in *Proc. IEEE Int. Conf. Acoust., Speech, Signal Process. (ICASSP)*, vol. 3, Mar. 2005, pp. iii/1129–iii/1132.
[37] M. Sadek, A. Tarighat, and A. H. Sayed, "Active antenna selection in multiuser MIMO communications," *IEEE Trans. Signal Process.*, vol. 55, no. 4, pp. 1498–1510, Apr. 2007.
[38] M. R. Dakkak, D. G. Riviello, A. Guidotti, and A. Vanelli-Coralli, "Evaluation of MU-MIMO digital beamforming algorithms in B5G/6G LEO satellite systems," in *Proc. 11th Adv. Satell. Multimedia Syst. Conf. 17th Signal Process. Space Commun. Workshop (ASMS/SPSC)*, Sep. 2022, pp. 1–8.
[39] P. Patcharamaneepakorn, S. Armour, and A. Doufexi, "On the equivalence between SLNR and MMSE precoding schemes with single-antenna receivers," *IEEE Commun. Lett.*, vol. 16, no. 7, pp. 1034–1037, Jul. 2012.
[40] N. Kim, Y. Lee, and H. Park, "Performance analysis of MIMO system with linear MMSE receiver," *IEEE Trans. Wireless Commun.*, vol. 7, no. 11, pp. 4474–4478, Nov. 2008.
[41] A. Alkhateeb, O. El Ayach, G. Leus, and R. W. Heath, "Hybrid precoding for millimeter wave cellular systems with partial channel knowledge," in *Proc. Inf. Theory Appl. Workshop (ITA)*, Feb. 2013, pp. 1–5.
[42] I. Ahmed, H. Khammari, A. Shahid, A. Musa, K. S. Kim, E. De Poorter, and I. Moerman, "A survey on hybrid beamforming techniques in 5G: Architecture and system model perspectives," *IEEE Commun. Surveys Tuts.*, vol. 20, no. 4, pp. 3060–3097, 4th Quart., 2018.
[43] J. Mo and R. W. Heath, "Capacity analysis of one-bit quantized MIMO systems with transmitter channel state information," *IEEE Trans. Signal Process.*, vol. 63, no. 20, pp. 5498–5512, Oct. 2015.

[44] J. Mo, P. Schniter, N. G. Prelcic, and R. W. Heath, "Channel estimation in millimeter wave MIMO systems with one-bit quantization," in *Proc. 48th Asilomar Conf. Signals, Syst. Comput.*, Nov. 2014, pp. 957–961.
[45] T. Lin, J. Cong, Y. Zhu, J. Zhang, and K. Ben Letaief, "Hybrid beamforming for millimeter wave systems using the MMSE criterion," *IEEE Trans. Commun.*, vol. 67, no. 5, pp. 3693–3708, May 2019.
[46] D. H. N. Nguyen, L. B. Le, T. Le-Ngoc, and R. W. Heath, "Hybrid MMSE precoding and combining designs for mmWave multiuser systems," *IEEE Access*, vol. 5, pp. 19167–19181, 2017.
[47] A. Kalachikov and A. Stenin, "Performance evaluation of the SRS based MIMO channel estimation on 5G NR open source channel model," in *Proc. IEEE 22nd Int. Conf. Young Professionals Electron Devices Mater. (EDM)*, Jun. 2021, pp. 124–127.
[48] *Proposal on SRS Estimation Error Modeling*, Standard r1-145389, 3GPP TSG RAN WG1 # 79, San Francisco, CA, USA, Nov. 2014.
[49] D. G. Riviello. MU-MIMO With Cylindrical Arrays and 3GPP TR 38.901 Channel Model MATLAB Simulator. GitLab. Accessed: Oct. 3, 2024. [Online]. Available: https://gitlab.com/daniel.riviello/mu-mimo-with-cylindrical-arrays-3gpp-tr-38.901-channel-model
[50] H. Martin, *Stochastic Geometry for Wireless Networks*. Cambridge, U.K.: Cambridge Univ. Press, 2012.
[51] S. Srinivasa and M. Haenggi, "Distance distributions in finite uniformly random networks: Theory and applications," *IEEE Trans. Veh. Technol.*, vol. 59, no. 2, pp. 940–949, Feb. 2010.
[52] T. Bai and R. W. Heath, "Coverage and rate analysis for millimeter-wave cellular networks," *IEEE Trans. Wireless Commun.*, vol. 14, no. 2, pp. 1100–1114, Feb. 2015.
[53] Q.-U.-A. Nadeem, A. Kammoun, M. Debbah, and M.-S. Alouini, "Design of 5G full dimension massive MIMO systems," *IEEE Trans. Commun.*, vol. 66, no. 2, pp. 726–740, Feb. 2018.
[54] A. I. Tunali and H. A. Çirpan, "Impact of imperfect channel estimation on 5G-NR," in *Proc. IEEE Int. Black Sea Conf. Commun. Netw. (BlackSeaCom)*, May 2021, pp. 1–6.
[55] *Physical Channels and Modulation (Release 15) V15.2.0*, Standard TS 38.211 3GPP, Sophia Antipolis, France, 2018.
[56] E. Björnson, J. Hoydis, M. Kountouris, and M. Debbah, "Massive MIMO systems with non-ideal hardware: Energy efficiency, estimation, and capacity limits," *IEEE Trans. Inf. Theory*, vol. 60, no. 11, pp. 7112–7139, Nov. 2014.
[57] C. Studer, M. Wenk, and A. Burg, "MIMO transmission with residual transmit-RF impairments," in *Proc. Int. ITG Workshop Smart Antennas (WSA)*, Feb. 2010, pp. 189–196.
[58] C. Yang, "An enhanced leakage-based precoding scheme for multi-user multi-layer MIMO systems," 2014, *arXiv:1407.3866*.
[59] B. Ren, M. Wang, C. Yang, L. Wang, J. Zou, T. Liu, and W. Yang, "An improved leakage-based precoding scheme for multi-user MIMO systems," in *Proc. IEEE 77th Veh. Technol. Conf. (VTC Spring)*, Jun. 2013, pp. 1–4.
[60] *User Equipment (UE) Radio Transmission and Reception; Part 2: Range 2 Standalone V17.5.0*, Standard TS 38.101-2, 3GPP, Sophia Antipolis, France, 2022.
[61] *Study on New Radio Access Technology: Radio Frequency (RF) and Co-existence Aspects V14.2.0*, Standard TR 38.803, 3GPP, Sophia Antipolis, France, 2017.



DANIEL GAETANO RIVIELLO (Member, IEEE) received the master's degree (magna cum laude) in telecommunications engineering and the Ph.D. degree in electronics and communications engineering from the Politecnico di Torino, Italy, in 2012 and 2016, respectively. He was a Research Fellow, in 2017, with Politecnico di Milano (in collaboration with Huawei Technologies Italia), from 2018 to 2020, with Politecnico di Torino (in collaboration with TIM), and from 2021 to 2024, with the Department of Electrical, Electronic, and Information Engineering "Guglielmo Marconi," University of Bologna. He is currently a Research Assistant and an Adjunct Professor with the Department of Electronics and Telecommunications, Politecnico di Torino. His research interests include wireless communication systems and include massive MIMO and beamforming techniques, array processing, and radio resource management for terrestrial and non-terrestrial networks. He is co-recipient of three best paper awards.



RICCARDO TUNINATO (Graduate Student Member, IEEE) received the bachelor's degree in electronic and computer engineering from the Universitã degli Studi di Trieste, in 2018, and the master's degree (cum laude) in communications and computer networks engineering from the Politecnico di Torino, in 2020, where he is currently pursuing the Ph.D. degree with the Department of Electronics and Telecommunications Engineering. His main research interest includes study and analysis of the physical layer of communication systems, mainly related to the 5G standard. In particular, he investigated the techniques for synchronization and initial access and the beamforming techniques for massive MIMO systems, with the support and collaboration of TIM.



ROBERTO GARELLO (Senior Member, IEEE) received the Ph.D. degree in electronic engineering from the Politecnico di Torino, in 1994, with a thesis on error correction coding. During the Ph.D. degree, he was a Visiting Student with MIT, Cambridge, and ETH Zürich. From 1994 to 1997, he was with Marconi Communications, Genoa. From 1998 to 2001, he was an Associate Professor with the University of Ancona. Since November 2001, he has been an Associate Professor with the Department of Electronics and Telecommunications, Politecnico di Torino. In 2017, he was an Adjunct Professor with California State University, Los Angeles. His main research interests include space communication systems, 5G and beyond mobile networks, and channel coding. On these topics, he has co-authored more than 150 articles. He has been the project manager of more than 40 research projects and the advisor of 12 Ph.D. students.

Open Access funding provided by 'Politecnico di Torino' within the CRUI CARE Agreement